# Stress dependence of the pocket gap modes in KI:$Ag^+$

A. Rosenberg, C. E. Mungan, and A. J. Sievers
*Laboratory of Atomic and Solid State Physics and Materials Science Center, Cornell University, Ithaca, New York 14853-2501*

K. W. Sandusky and J. B. Page
*Department of Physics and Astronomy, Arizona State University, Tempe, Arizona 85287-1504*

(Received 1 April 1992)

Far-ir uniaxial-stress experiments reveal the unusual result that the pocket gap modes in KI:$Ag^+$ couple much more to the fully symmetric ($A_{1g}$) strain than to the tetragonal ($E_g$) and trigonal ($T_{2g}$) strains; other modes due to monatomic substitutional defects are found to couple with similar strengths to both $A_{1g}$ and $E_g$ strains. Theoretical calculations based on perturbed breathing-shell-model phonons and a simple anharmonicity model suggest the presence of unusual pressure-induced microscopic displacements in the vicinity of the defect's fourth-nearest neighbors. The coupling coefficients of the pocket gap mode at 86.2 $cm^{-1}$ are measured to be temperature dependent, with the $E_g$ coefficient actually changing sign at 12 K; such behavior has not been found for other impurity-induced localized modes.

## I. INTRODUCTION

At first sight, the spectroscopic data describing the defect dynamics of the $Ag^+$ impurity in KI or RbCl appear readily interpretable: The low-frequency resonant mode associated with $Ag^+$ in KI is representative of an on-center impurity,[1] while the tunneling levels for $Ag^+$ in RbCl are characteristic of an impurity ion that is off center with respect to the normal lattice site.[2–6] However, systematic experimental studies of both of these lattice-defect systems have led to the discovery of a number of unexpected vibrational characteristics.[6–10] Prominent among these is the near instability of the $Ag^+$ ion in both systems.

For the RbCl host, a modest hydrostatic pressure tunes the on-center configuration into the same energy range as the off-center one. In paraelectric resonance studies over a narrow hydrostatic pressure range, microwave transitions have been observed between the off- and on-center configurations.[7] The integrated strengths of these transitions decrease much more rapidly with increasing temperature than population effects predict.[8]

For the KI host, the low-temperature dynamics of the $Ag^+$ ion show drastic but analogous temperature-dependent changes in the characteristic far-ir,[9] radio-frequency,[10] uv,[11] and Raman[11] spectra with temperature. The strengths of the impurity-induced vibrational modes observed with far-ir or Raman techniques vanish when the system is heated to approximately 25 K, with the simultaneous appearance of several new modes associated with the high-temperature configuration.

The results for both $Ag^+$-defect systems are consistent with the local arrangement of the impurity and its surroundings being in one of two possible configurations: For KI, these are a low-temperature on-center configuration and a high-temperature off-center configuration; for RbCl, the low-temperature configuration is an off-center one, with a hydrostatic-pressure-induced on-center configuration nearby in energy. A surprising feature common to both of these $Ag^+$-defect systems is that the strengths of the characteristic spectroscopic transitions can completely disappear with increasing temperature at a rate much faster than expected from population effects, indicating that the high-temperature configuration must have a much larger number of available states than the low-temperature one.

Because the low-temperature KI:$Ag^+$ on-center impurity system presents fewer parameters in a comparison between theory and experiment than does the off-center RbCl:$Ag^+$ system, we have focused our attention in recent years on determining whether or not a harmonic model using perturbed breathing-shell-model (BSM) phonons[12] can account for the unusual low-temperature experimental results in KI:$Ag^+$. In our initial effort, we found that the measured frequencies and relative strengths of the resonant and gap modes observed for the zero-temperature on-center configuration of KI:$Ag^+$ can be described accurately within the framework of perturbed BSM phonons.[11] When the perturbed BSM phonons are fit to the observed frequencies of the strong ir-active resonant and gap modes of KI:$Ag^+$ at 17.3 and 86.2 $cm^{-1}$, respectively, the model predicts the existence of three different-symmetry gap modes of nearly equal frequencies.[13] These are a nondegenerate $A_{1g}$ mode at 87.2 $cm^{-1}$, a twofold-degenerate $E_g$ mode at 86.0 $cm^{-1}$, and the threefold-degenerate $T_{1u}$ ir-active mode at 86.2 $cm^{-1}$. The calculated displacement patterns for these modes are shown in Figs. 1(a)–1(c). All of the displacement patterns for these modes essentially involve only motion of the defect's fourth-nearest neighbors, as noted by the positions of the dashed circles in Fig. 1. The nearly degenerate frequencies of these modes result from the local dynamics within each of the fourth-nearest-neighbor "pockets," which are weakly coupled to produce the different-symmetry modes. We shall refer to these modes as "pocket gap modes." For contrast, Fig.

 

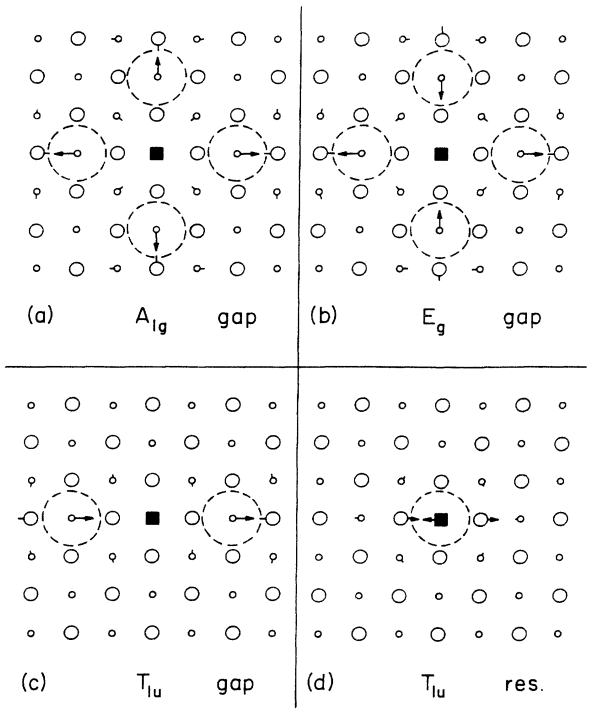


FIG. 1. Calculated displacement patterns in the $x$-$y$ plane for different KI:$Ag^+$ modes. (a) 87.2-$cm^{-1}$ $A_{1g}$ pocket gap mode. (b) 86.0-$cm^{-1}$ $E_g(1)$ pocket gap mode. (c) 86.2-$cm^{-1}$ $T_{1u}(x)$ pocket gap mode. (d) 17.3-$cm^{-1}$ $T_{1u}(x)$ resonant mode. Here $T_{1u}(x)$ denotes the $T_{1u}$ partner which couples to $\hat{x}$-polarized radiation and $E_g(1)$ denotes one of the two degenerate $E_g$ partners. Note that the displacement pattern for the resonant mode is peaked on the defect and its nearest neighbors, while the displacement patterns for the pocket gap modes [(a)–(c)] are peaked on the fourth-neighbor sites, away from the defect. The displacements for the different symmetries are not drawn to scale.

1(d) shows the computed displacement pattern for one partner of the threefold-degenerate 17.3-$cm^{-1}$ $T_{1u}$ resonant mode, whose displacements are essentially confined to the defect and its nearest neighbors.

The apparent correctness of the model was strengthened recently by the prediction and subsequent observation of a large host-induced splitting in the gap-mode spectrum as a result of the presence of the two most abundant naturally occurring $K^+$ isotopes. This spectroscopic signature is caused by the unusual pocket nature of the gap-mode displacement patterns.[13] However, the observed rapid temperature dependence of the entire impurity-induced spectrum suggests that the defect system must be strongly anharmonic in some way. Since some experimental and theoretical results are compatible with a harmonic model while the observed temperature dependence of the line strengths suggest a strong anharmonic behavior, the correct picture of the underlying dynamics of KI:$Ag^+$ remains a puzzle.

To examine the size and properties of the anharmonicity in the low-temperature on-center configuration, we have extended the earlier uniaxial-stress measurements on the resonant mode[14] to the higher-frequency ir-active pocket gap mode. We measured the effect of uniaxial stress on these modes, as well as on "standard" gap modes produced by the monatomic substitutional defects $Cl^-$, $F$ centers, $Cs^+$, and $Rb^+$ in the same host, KI, at low temperatures. Moreover, the temperature dependence of the pocket-mode stress dependence was studied; we have found that the $A_{1g}$ and $E_g$ coupling coefficients are both temperature dependent, with the $E_g$ coefficient actually changing sign at 12 K. Such temperature-dependent behavior is not found for other impurity-induced localized modes.

The main theoretical purpose of this work is to determine whether or not the previously successful harmonic model used to describe the experimental results in Refs. 11 and 13 can be extended to account for the unusual stress shifts measured for the KI:$Ag^+$ pocket gap modes, reported here. In particular, we would like to determine the anharmonic potential-energy terms near the pockets from the stress data. By comparing the measured stress-induced frequency shifts with the predictions of a simple anharmonic extension of our defect model, we find that the on-center $Ag^+$ configuration gap mode has an overall anharmonicity comparable to or somewhat smaller than that of gap modes caused by other point defects in KI, as reflected in the stress coupling coefficients. However, it is unusual in that the anharmonic coupling is predominantly to $A_{1g}$ strains.

In the next section, the uniaxial-stress apparatus and experimental techniques are described. The experimental results are presented in Sec. III. It is found that the qualitative uniaxial-stress behavior of the standard gap modes, whose displacement patterns are localized at or near the defect sites, differs from that of the pocket gap modes. Our anharmonically extended breathing-shell model is introduced in Sec. IV. To relate the stress response to the anharmonicity, a quasiharmonic model is assumed in which frequency shifts linear in stress arise from force-constant changes caused by the stress-induced local strains via third-order anharmonicities. The calculation of the stress coupling coefficients follows. The experimental and theoretical findings are discussed in Sec. V, where the analysis of the KI:$Ag^+$ pocket-mode stress shifts suggests the presence of unusual pressure-induced microscopic displacements in the vicinity of the defect's fourth-nearest neighbors. Section VI presents the general conclusions. A more detailed discussion of the stress-shift theory is given in the Appendix.

## II. EXPERIMENTAL TECHNIQUES

### A. Samples

The pure KI starting material, doped with AgI in nominal concentrations ranging from 0.1 to 0.5 mol %, was grown into crystals by the Czochralski method at the Cornell Materials Science Center Crystal Growing Facility; the crystals used are identified in Table I. A careful spectroscopic study of the crystals in the region of the KI phonon gap shows that the spectral structure is dependent on the KI source material;[15] thus, some care is required in choosing this material. We have found that

TABLE I. Identification of crystals used in this study. The AgI content listed is that of the melt.

| Boule no. | Identification no. | Nominal composition |
|---|---|---|
| 1 | 9012144W | KI+0.1 mol% AgI |
| 2 | 9106255W | KI+0.1 mol% AgI |
| 3 | 9101164W | KI+0.4 mol% AgI |
| 4 | 9111065W | KI+0.5 mol% AgI |
| 5 | 805235 | KI+0.5 mol% AgI |
| 6 | 8711185W | KI |

some nominally pure KI contains naturally occurring $Rb^+$, which gives rise to KI:$Rb^+$ gap modes at nearly the same frequency as the KI:$Ag^+$ pocket gap modes of interest here. These gap-mode features are shown in Fig. 2 at a resolution of 0.1 $cm^{-1}$. The spectrum showing the KI:$Ag^+$ modes is labeled *B*, and the spectrum showing the modes caused by the two isotopes of $Rb^+$ is labeled *A*; these KI:$Rb^+$ gap modes are identified here for the first time. The weak KI:$Ag^+$ absorption line at 84.5 $cm^{-1}$ in *B* results from the mixing of the nearly degenerate $A_{1g}$, $E_g$, and $T_{1u}$ pocket gap modes caused by the naturally occurring 7% isotopic abundance of $^{41}K$ in the KI host.[13] This mode, whose displacement pattern involves a single pocket,[13] will be referred to as the "KI:$Ag^+$ isotope mode."

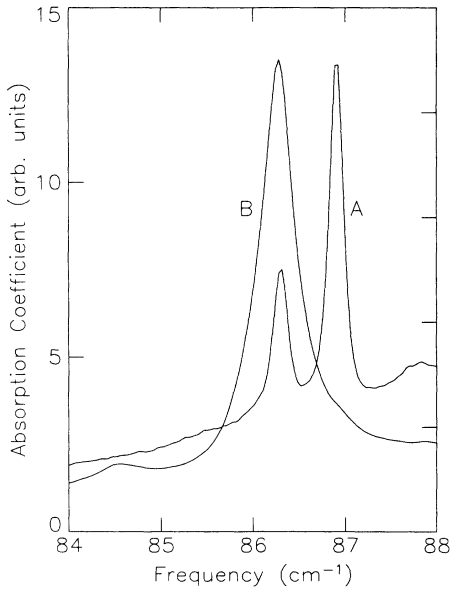


FIG. 2. Absorption coefficient at 1.7 K over part of the phonon gap region of KI. Curve *A* is a spectrum of nominally pure KI (No. 6 in Table I), showing the gap-mode doublet at 86.3 and 86.9 $cm^{-1}$ caused by naturally occurring $Rb^+$ (the $Rb^+$ concentration is not known); curve *B* is a spectrum of KI+0.4 mol% AgI (No. 3 in Table I), showing the pocket gap and isotope modes caused by $Ag^+$ at 86.2 and 84.5 $cm^{-1}$, respectively. (The KI starting material for the "pure" sample, containing $Rb^+$, was of a lower-purity grade than that used for the KI:$Ag^+$ samples; see Ref. 15.) The resolution of these spectra is 0.1 $cm^{-1}$. The isotope splitting for KI:$Rb^+$, observed here for the first time, is due to the natural abundance of $^{87}Rb$ (28%) and $^{85}Rb$ (72%); the line at 86.9 $cm^{-1}$ is 2.7× stronger than the one at 86.3 $cm^{-1}$, and the FWHM of each line (Ref. 16) is 0.14 $cm^{-1}$. Note that the KI:$Ag^+$ modes are significantly broader than the KI:$Rb^+$ ones.

Measurements on the "standard" gap modes caused by the $Cl^-$ and $Cs^+$ in KI were performed on KI:$Ag^+$ samples containing these defects as naturally occurring impurities. The *F* centers ($e^-$) were produced in undoped KI crystals by irradiating them at room temperature with 4 eV radiation from an excimer laser.[17]

The samples used for the [100] stress measurements were cleaved from the boule to a thickness of 2–10 mm and slightly wedged to avoid channel spectra; the samples used for the [110] stress measurements were sanded to the correct orientation after cleaving. Aggregates of AgI, which build up in a crystal with time at room temperature, were dispersed just before cooling each sample by heating it to ~200 °C and quenching it back to room temperature.

### B. Uniaxial-stress apparatus

The cryostat insert used to apply uniaxial stress is shown in Fig. 3. A balanced set of weights hang on lever arms with a 12:1 mechanical advantage and, external to the cryostat, push down on a piston, which in turn pushes on the sample. The lower part of the piston is separated from the upper part by a ball bearing in order to maintain the vertical direction of the force at the sample. Cardboard spacers are placed on the top and bottom

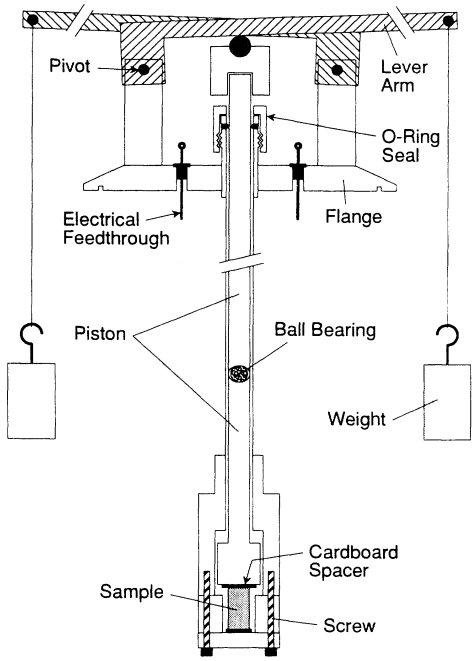


FIG. 3. Schematic view of the uniaxial-stress cryostat insert. The weights hang on lever arms external to the cryostat. The flange seals the top of the cryostat sample chamber. The force is transmitted to the sample by a piston which enters the cryostat through an o-ring seal. Cardboard spacers are used on the top and bottom of the sample to distribute the pressure uniformly. An electrical feedthrough allows temperature measurements by connecting to a calibrated carbon resistor near the sample. The total length of the insert is ~1 m (not to scale).

surfaces of the sample to distribute the pressure uniformly. The weights used ranged up to 7 kg on each arm, depending on the cross-sectional area of the particular sample. The maximum stress, beyond which the samples tended to shatter, was found to be $\sim 3.5\times10^7$ N/m$^2$ for [100]-oriented crystals and $\sim 2.5\times10^7$ N/m$^2$ for [110]-oriented crystals. An electrical feedthrough at the top of the uniaxial-stress cryostat insert allowed temperature measurement through a calibrated Allen-Bradley resistor located next to the sample.

### C. Transmission measurements

Transmission spectra were taken with a rapid-scan Fourier-transform interferometer at resolutions of 0.05–1 cm$^{-1}$. A wire grid polarizer on a polyethylene substrate was used to measure spectra with the incident radiation polarized parallel and perpendicular to the applied stress direction. The samples were placed in a liquid-helium immersion cryostat which had room- and helium-temperature polypropylene windows. The construction of the cold windows, illustrated in Fig. 4, is similar to that described in Ref. 18, but is perhaps more versatile because the windows are not glued directly to the cryostat, making their replacement easier. The cold windows must be replaced periodically because of repeated temperature cycling or aging of the epoxy seal.

The construction of the polypropylene cold windows shown in Fig. 4 is more complex than that of Mylar ones because polypropylene is much more difficult to seal with epoxy. The Mylar windows are generally made by epoxying the Mylar film between two brass washers and then soldering the assembly to the cryostat.[19] A similar technique was found not to give satisfactory results with polypropylene. As a result, the method shown in Fig. 4 was developed, which prevents heating of the epoxy seals: First, the brass seats are soldered in the two window positions on either side of the sample chamber; second, the polypropylene film (cut into circles that fit inside the brass seats) and the brass retainer rings are epoxied in place; third, the epoxy is cured at room temperature.[20] The extra effort involved in this procedure is justified by the superiority of the ir transmission of polypropylene to that of Mylar.[18]

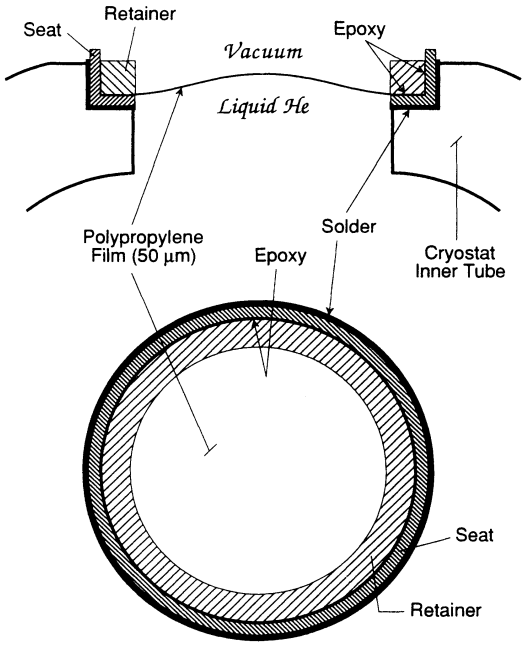


FIG. 4. Design of the polypropylene cold windows for the cryostat's sample chamber. The thin polypropylene film (50 μm) is sandwiched with epoxy between two concentric brass rings, the outer one being soldered to a counterbored hole in the cryostat's sample chamber. These windows have an overall diameter of 2.5 cm and a clear-view diameter of 1.9 cm (not to scale). A side view (upper panel) and a top view (lower panel) are shown. The assembly procedure is described in the text.

## III. EXPERIMENTAL RESULTS

Figure 5 gives the far-ir absorption coefficient in the phonon gap region of KI, showing modes associated with substitutional $Ag^+$, $Cl^-$, and $Cs^+$ defects. The resolution is 0.1 cm$^{-1}$. The absorption coefficient was obtained by taking the ratio of the spectra of two KI:$Ag^+$ crystals of the same concentration (KI+0.4 mol% AgI) having different thicknesses (2.9 and 1.3 mm). Although the dominant feature in Fig. 5 is the pocket gap mode at 86.2 cm$^{-1}$, other strong features can be seen, namely, the KI:$Cl^-$ gap-mode doublet at 76.8 and 77.1 cm$^{-1}$ (Ref. 1) and the KI:$Cs^+$ gap mode at 82.9 cm$^{-1}$.[1] ($Cl^-$ and $Cs^+$ are present in most of our samples as natural impurities.)

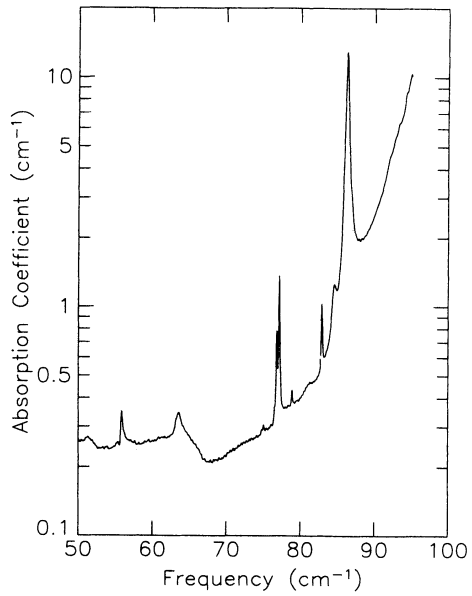


FIG. 5. Absorption coefficient of a sample of KI+0.4 mol% AgI in the gap below the optical-phonon region at 1.7 K. The resolution is 0.1 cm$^{-1}$. The dominant features are the KI:$Ag^+$ pocket gap mode at 86.2 cm$^{-1}$ and the gap modes due to KI:$Cl^-$ (76.8 and 77.1 cm$^{-1}$) and KI:$Cs^+$ (82.9 cm$^{-1}$); the latter are present as natural impurities (No. 3 in Table I). Additional weak features due to KI:$Ag^+$ are at 55.8, 63.6, and 84.5 cm$^{-1}$: All are associated with the on-center configuration of the $Ag^+$ impurity. (A weak mode is also visible at 78.9 cm$^{-1}$; its origin is unknown, but is not due to isolated $Ag^+$ ions.) Some properties of the KI:$Ag^+$ modes are summarized in Table II.

TABLE II. Far-ir modes due to the KI:$Ag^+$ low-temperature on-center configuration measured at 1.6 K. All strengths are given relative to that of the 86.2-$cm^{-1}$ gap mode.

| Frequency ($cm^{-1}$) | FWHM ($cm^{-1}$) | Relative strength | Identification |
|---|---|---|---|
| 55.8 | 0.29 | 0.006 | band mode |
| 63.6 | 1.9 | 0.024 | density-of-states feature |
| 84.5 | 0.5 | 0.04 | isotope pocket gap mode |
| 86.2 | 0.51 | 1.00 | pocket gap mode |

Note that the KI:$Ag^+$ pocket gap mode at 86.2 $cm^{-1}$ is substantially broader than the gap modes produced by other monatomic substitutional defects. In addition, Fig. 5 shows weak $Ag^+$ features in the acoustic-phonon region of KI at 55.8 and 63.6 $cm^{-1}$. The line at 55.8 $cm^{-1}$, previously observed at lower resolution[21] and assigned to a density of states feature,[9] is remarkable in that its full width at half maximum (FWHM) of 0.29 $cm^{-1}$ is smaller than that of the pocket gap mode even though it is located in the high-density-of-states region of the acoustic-phonon spectrum.[22] The frequencies, FWHM's, and relative strengths of these KI:$Ag^+$ modes are summarized in Table II.[16] When these results are compared with those in Table I of Ref. 21, it is found that in the earlier study neither the gap mode nor the 55.8-$cm^{-1}$ line were fully resolved. However, all of the KI:$Ag^+$ modes identified in both of these tables disappear as the temperature is increased to 25 K, indicating that they are all associated with the on-center configuration.[9] At higher temperatures other features appear which are associated with the off-center $Ag^+$ configuration.[9] In addition, host-crystal difference-band absorption then begins to play an important role in determining the absorption coefficient.[23]

Application of uniaxial stress causes the KI:$Ag^+$ features in Fig. 5 at 86.2, 84.5, and 55.8 $cm^{-1}$, as well as the KI:$Cl^-$ and KI:$Cs^+$ gap modes, to shift. The frequency shifts, which are linear in applied stress in the small-strain regime examined in this work, are smaller than 0.4 $cm^{-1}$ at the maximum applied stress; the actual magnitude depends on the polarization and stress direction relative to the crystallographic axes. Negligible changes in the linewidths are observed with applied stress.

Because the frequency shifts are often smaller than or comparable to the linewidths, especially in the case of the relatively broad KI:$Ag^+$ pocket gap modes, visual inspection of the positions of the maxima was found to be an insufficiently accurate technique for determining the sizes of the shifts. The accuracy of our determination has been increased by using a "global" analysis in the region of the lines, which takes fuller advantage of the available data.[24] The method consists of overlaying the shifted line at some given nonzero stress onto the corresponding line at zero stress and varying the position and width of the line at nonzero stress until the area between the two curves is minimized. This area is given by the integral

$$\int \left| \frac{\alpha_1(s\nu)}{\alpha_1^{\text{peak}}} - \frac{\alpha_2(\nu-\Delta\nu)}{\alpha_2^{\text{peak}}} \right| d\nu \tag{1}$$

as a function of the two variables $s$ and $\Delta\nu$, where the two absorption lines $\alpha_1(\nu)$ and $\alpha_2(\nu)$ have been normalized to unit height by dividing them by their maxima $\alpha_1^{\text{peak}}$ and $\alpha_2^{\text{peak}}$, respectively. The width of the first line relative to that of the second is then equal to $s$, and its frequency shift is related to $\Delta\nu$. A computer algorithm was implemented to perform this minimization.

After the frequency shift at each value of applied stress was determined, the shifts were plotted against the applied stress and the slope was obtained; this procedure was repeated for each polarization and stress direction for each spectral line. Since all of the defects of interest here are on center in the KI host cubic lattice at low temperatures (i.e., the defect replaces an ion in the host lattice at a normal lattice site), the slopes are linearly related to the compliances of the host through three coefficients $A$, $B$, and $C$, whose sizes are indicative of a particular mode's coupling to the fully symmetric (hydrostatic) ($A_{1g}$), tetragonal ($E_g$), and trigonal ($T_{2g}$) components of strain, respectively.[1,25] Since the compliances of bulk KI are known,[26] experimental values for the coupling coefficients can thus be determined. The equations relating the slopes to the compliances through the coupling coefficients are summarized in Table III for the cases of [100] and [110] applied stress.

In general, the [100] stress data, which were more accurate because of the higher achievable stress, were used to determine the $A$ and $B$ coupling coefficients, and the less-accurate [110] data were used to determine $C$ (see Table III). The scatter in the points determined the error bars associated with the slopes, which were propagated through the equations of Table III to obtain the errors in the coupling coefficients.

Figures 6(a) and 6(b) show the effects of [100] and [110] stress, respectively, on the position of the KI:$Ag^+$ 86.2-$cm^{-1}$ pocket gap mode at 1.7 K. There is a small shift to

TABLE III. Frequency shifts $\Delta\nu$ of the $T_{1u}$ states with applied uniaxial stress, $\Delta P$, along [100] and [110] crystal directions. The coefficients $A$, $B$, and $C$ describe the coupling of the $T_{1u}$ modes to $A_{1g}$, $E_g$, and $T_{2g}$ strains, respectively. The $S_{\alpha\beta}$'s are compliances of the host lattice (KI); their values at 4.2 K are $S_{11}+2S_{12}=2.62\times10^{-11}$ $m^2/N$, $S_{11}-S_{12}=3.16\times10^{-11}$ $m^2/N$, and $S_{44}=27.2\times10^{-11}$ $m^2/N$ (from Ref. 26).

| Stress | Polarization | $-\Delta\nu/\Delta P$ |
|---|---|---|
| 100 | 100 | $A(S_{11}+2S_{12})+4B(S_{11}-S_{12})$ |
| 100 | 010 | $A(S_{11}+2S_{12})-2B(S_{11}-S_{12})$ |
| 110 | 110 | $A(S_{11}+2S_{12})+B(S_{11}-S_{12})+CS_{44}/2$ |
| 110 | 1-10 | $A(S_{11}+2S_{12})+B(S_{11}-S_{12})-CS_{44}/2$ |

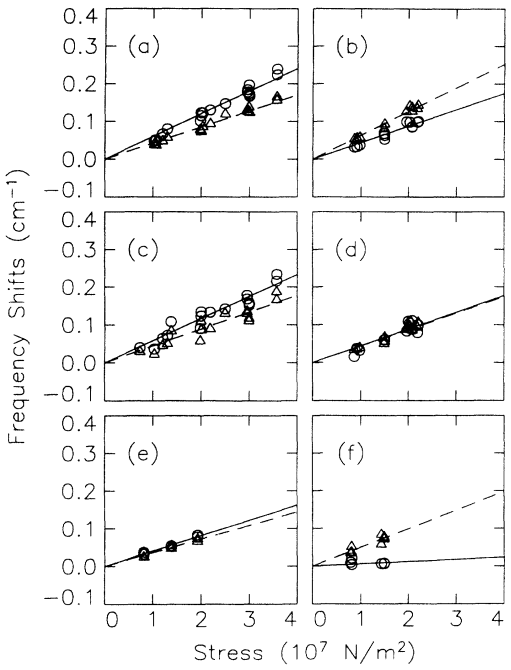


FIG. 6. Frequency shifts of KI:$Ag^+$ on-center configuration modes between 1.7 and 4 K induced by uniaxial stress. The 86.2-cm$^{-1}$ pocket gap mode: (a) [100] stress and (b) [110] stress (Nos. 1, 2, and 3 in Table I). The 84.5-cm$^{-1}$ isotope gap mode: (c) [100] stress and (d) [110] stress (Nos. 2, 3, 4, and 5 in Table I). The 55.8-cm$^{-1}$ mode: (e) [100] stress and (f) [110] stress (Nos. 3, 4, and 5 in Table I). The circles (triangles) are the data, and the solid (dashed) lines are the best fits for polarization parallel (perpendicular) to the stress direction. (For [110] stress the perpendicular polarization is along [1-10].)

higher frequency for both parallel and perpendicular polarizations in both stress directions. The small size of the difference between the slopes for the two polarizations in the [100] stress direction is unusual: Combined with the similar [110] result, it implies that this mode couples almost exclusively to fully symmetric strains, i.e., that the $A$ coupling coefficient is much greater than both the $B$ and $C$ coefficients (see Table IV), although none of the coefficients for this mode is zero within experimental error. Similar results are found for the isotope gap mode at 84.5 cm$^{-1}$, as shown in Figs. 6(c) and 6(d); for this mode, the $C$ coefficient is found to be zero within experimental error.

The stress results for the sharp 55.8-cm$^{-1}$ KI:$Ag^+$ band mode are shown in Figs. 6(e) and 6(f). Although the qualitative behavior of this mode is similar to that of the pocket gap modes in Figs. 6(a)–6(d), the stress shifts for the 55.8-cm$^{-1}$ mode are significantly smaller, indicating a weaker coupling to the applied stress than that of the pocket gap modes. There are additional subtle differences between this mode's stress behavior and that of the pocket modes (see Table IV): Namely, the $B$ coefficient of this mode is zero within experimental error, while the magnitude of its $C$ coefficient is slightly larger than for the pocket gap modes.

For comparison to the KI:$Ag^+$ pocket gap modes, we have measured the stress behavior of some "standard" gap modes produced by other monatomic substitutional defects in KI. We find that the behavior of these gap modes is qualitatively different from that of the KI:$Ag^+$ pocket gap modes. For example, the stress dependences of the 77.1-cm$^{-1}$ KI:$Cl^-$, 82.9-cm$^{-1}$ KI:$Cs^+$, and 86.9-cm$^{-1}$ KI:$Rb^+$ gap modes are shown in Fig. 7: For [100] stress the shifts are very different for the two orthogonal polarizations, unlike the case of the KI:$Ag^+$ pocket gap modes [compare Figs. 7(a), 7(c), and 7(e) with Figs. 6(a), 6(c), and 6(e)]. This large difference between the two polarizations for [100] stress implies significant coupling to tetragonal strains for standard gap modes, in addition to the coupling to the fully symmetric strains. Inspection of the coupling coefficients collected in Table IV reveals similar behavior for all standard impurity gap modes in KI. This suggests that a small $B/A$ ratio is a stress-behavior signature of the pocket gap modes, which sets them apart from the standard gap modes.

TABLE IV. Measured values of the stress coupling coefficients of the ir-active gap and resonant modes of the KI:$Ag^+$, KI:$Cl^-$, KI:$e^-$, KI:$Cs^+$, and KI:$Rb^+$ defect systems. Note that $B/A$ nearly vanishes for the first two modes, which are pocket modes, and for the 55.8-cm$^{-1}$ KI:$Ag^+$ mode in the acoustic spectrum. On the other hand, the KI:$Ag^+$ resonant mode at 17.3 cm$^{-1}$ and the last six "standard" gap modes have much larger values of $B/A$. The stress coupling coefficients are given in units of cm$^{-1}$/unit strain. The measurements were made between 1.7 and 3.5 K.

| Mode | Frequency (cm$^{-1}$) | $A$ | $B$ | $C$ | $B/A$ |
|---|---|---|---|---|---|
| KI:$Ag^+$ | 86.2 | 186±21 | 9±6 | −7±6 | 0.05±0.03 |
| KI:$Ag^+$ | 84.5 | 188±22 | 7±6 | 0±6 | 0.04±0.03 |
| KI:$Ag^+$ | 55.8 | 143±32 | 2±9 | −16±9 | 0.01±0.06 |
| KI:$Ag^+$ [a] | 17.3 | 390±90 | 510±70 | −15±10 | 1.31±0.35 |
| KI:$Cl^-$ | 76.8 | 102±36 | 53±10 | −19±10 | 0.52±0.21 |
| KI:$Cl^-$ | 77.1 | 101±36 | 55±10 | −20±10 | 0.54±0.22 |
| KI:$e^-$ | 82.7 | 143±55 | 39±18 | −20±15 | 0.27±0.16 |
| KI:$Cs^+$ | 82.9 | 148±56 | 80±15 | −20±15 | 0.54±0.23 |
| KI:$Rb^+$ | 86.3 | 147±55 | 69±14 | −21±15 | 0.47±0.20 |
| KI:$Rb^+$ | 86.9 | 143±55 | 68±14 | −20±15 | 0.48±0.21 |

[a]From Ref. 14.

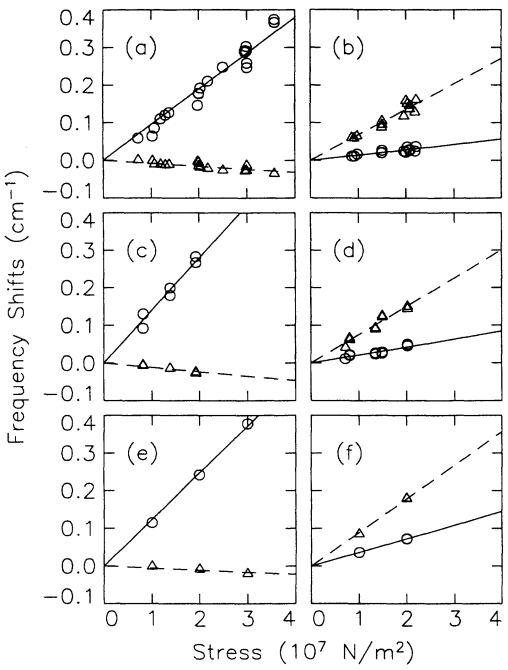


FIG. 7. Frequency shifts of several "standard" gap modes at 1.7 K induced by uniaxial stress. The 77.1-$cm^{-1}$ KI:$Cl^-$ mode: (a) [100] stress and (b) [110] stress (Nos. 2 and 3 in Table I). The 82.9-$cm^{-1}$ KI:$Cs^+$ mode: (c) [100] stress and (d) [110] stress (No. 3 in Table I). The 86.9-$cm^{-1}$ KI:$Rb^+$ mode: (e) [100] stress and (f) [110] stress (No. 6 in Table I). The circles (triangles) are the data, and the solid (dashed) lines are the best fits for polarization parallel (perpendicular) to the stress direction. (For [110] stress, the perpendicular polarization is along [1-10].)

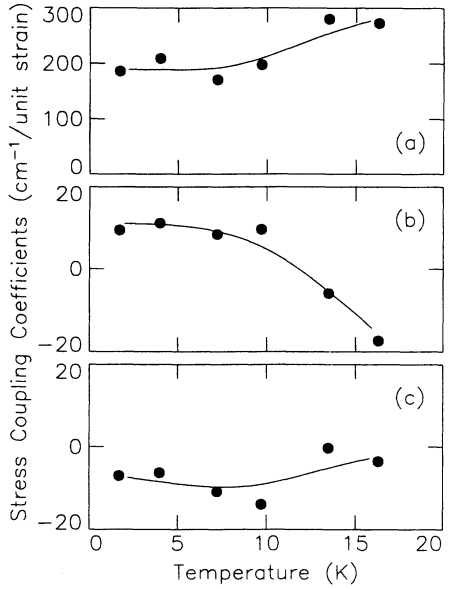


FIG. 8. Temperature dependence of the stress coupling coefficients of the 86.2-$cm^{-1}$ KI:$Ag^+$ pocket gap mode. Identification: (a) fully symmetric $A$ coefficient, (b) tetragonal $B$ coefficient, and (c) trigonal $C$ coefficient (Nos. 3 and 5 in Table I). The circles are the experimental points, and the lines are guides to the eye.

To further emphasize the fundamental difference between the stress results for the pocket gap modes and the results for modes due to other point defects, we note that a relatively large $B/A$ ratio is found for local modes above the LO-phonon region in other defect systems,[1] as well as for the low-frequency 17.3-$cm^{-1}$ KI:$Ag^+$ resonant mode (see Table IV). These examples demonstrate the unique nature of the stress behavior of the KI:$Ag^+$ pocket gap mode, the related isotope mode, and the 55.8-$cm^{-1}$ band mode. Note that the values of the $A$ coefficients of the KI:$Ag^+$ and KI:$Cl^-$ gap modes reported here are in good agreement with previous hydrostatic stress measurements.[27] The $A$ and $B$ coefficients reported for $F$ centers in KI are in good agreement with the results of a previous uniaxial-stress study.[28]

The discovery of the 55.8-$cm^{-1}$ KI:$Ag^+$mode, which is not predicted by our BSM calculations and whose origin is not understood, is indeed intriguing; it is the narrowest line produced by the KI:$Ag^+$ on-center configuration, in spite of the fact that it is located in the high-density-of-states acoustic-phonon region of KI. The fact that this mode shares the small $B/A$-ratio stress signature of the KI:$Ag^+$ pocket gap and isotope modes suggests that it too may have a pocket-type displacement pattern.

The weak and broad 63.6-$cm^{-1}$ KI:$Ag^+$ mode, shown in the spectrum of Fig. 5, has no measurable stress shifts within experimental error. This mode, like the 55.8-$cm^{-1}$ KI:$Ag^+$ mode discussed above, is also not predicted by the shell-model calculations and its origin is not understood. This lack of coupling to *any* strain symmetry has not been observed previously for any resonant, gap, or local modes.

The only mode whose stress coefficients are found to have significant temperature dependence in this restricted temperature region is the KI:$Ag^+$ pocket gap mode at 86.2 $cm^{-1}$; the results are shown in Fig. 8. At about 12 K, the $B$ coefficient goes to zero and then becomes increasingly negative upon raising the temperature still further. Also, at about 12 K, the $A$ coefficient starts to grow, while the $C$ coefficient begins to approach zero. The sign change of the $B$ coefficient is the most striking temperature dependence ever observed for the stress behavior of any localized defect mode. The temperature dependence of the stress coefficients of the related isotope gap mode at 84.5 $cm^{-1}$ could not be studied because this mode is not resolved from the 86.2-$cm^{-1}$ mode at higher temperatures due to the increased linewidth. For the 55.8-$cm^{-1}$ KI:$Ag^+$ mode, the only temperature dependence observed is a slight increase in the magnitude of $A$ with increasing temperature; this is similar to the characteristic behavior of the standard KI gap modes mentioned above. Thus the temperature dependence of the 86.2-$cm^{-1}$ KI:$Ag^+$ pocket-gap-mode stress coefficients is unique among all modes measured to date.

## IV. THEORY

### A. Model

The parameters which characterize the perturbed BSM phonons,[11] include the defect mass, defect-nearest-

neighbor (0-1$n$) longitudinal force-constant changes $\delta$, and relaxation-induced 1$n$-4$n$ longitudinal force-constant changes $\delta'$. All other long- and short-range force constants are unperturbed. The force-constant changes $\delta$ and $\delta'$ are fit to the observed $T_{1u}$ resonant and gap modes at 17.3 and 86.2 $cm^{-1}$, respectively, yielding the values given in the first row of Table V. The model then predicts an $E_g$ resonant mode at 20.5 $cm^{-1}$, in fair agreement with the observed Raman-active mode at 16.1 $cm^{-1}$.[11,21] Moreover, as discussed in the Introduction, the model also predicts nearly degenerate pocket gap modes of three different symmetries ($A_{1g}$, $E_g$, and $T_{1u}$). Table V summarizes some of the important predictions of the harmonic-defect model.

While the low-temperature far-ir and Raman spectra, as well as the gap-mode isotope splitting, are well described by our harmonic-defect model,[11,13] the stress-induced frequency shifts reflect *anharmonic* terms in the potential energy. Our procedure for calculating the stress-induced frequency shifts is schematically outlined in Fig. 9 and is described below. Details of the calculation are presented in the Appendix.

To relate the stress to the anharmonicity, we adopt a quasiharmonic model in which frequency shifts linear in stress arise from force-constant changes caused by the stress-induced local strains via third-order anharmonicities. The stress-induced force-constant changes do not couple even- and odd-parity modes, and so the stress shifts for the ir-active gap mode at 86.2 $cm^{-1}$ are determined by a degenerate perturbation calculation involving only the three degenerate ir-active $T_{1u}$ pocket gap modes.

Unlike the $T_{1u}$ pocket gap modes, the 84.5 $cm^{-1}$ KI:$Ag^+$ *isotope* mode is a linear combination of the odd-parity $T_{1u}$ and even-parity $E_g$ and $A_{1g}$ pocket gap modes.[13] Thus, in principle, the calculation of the isotope-mode stress shifts should involve pocket gap modes of all three symmetry types. However, since the stress-induced frequency shifts are less than a factor of 0.2 smaller than the $\sim 1.5$-$cm^{-1}$ separation between the isotope and main gap modes, we can use nondegenerate perturbation theory to determine the isotope-mode stress shifts.

The local strains needed for the theory are the stress-induced ionic displacements in the defect crystal. These will be strongly affected by the zero-stress harmonic force-constant changes ($\delta$,$\delta'$) in our model. By comparing the expressions for the response to a given stress acting on the defect crystal and on the pure crystal, Elliot, Krumhansl, and Merrett[29] have shown how to relate the microscopic defect-crystal strains to their pure-crystal counterparts, using zero-frequency perturbed harmonic Green's functions. As a result, the external stresses can be readily converted to the local ionic displacements near the defect.

Since the largest stress-induced force-constant changes should originate from the strong and rapidly varying short-range overlap forces, we will only consider nearest-neighbor anharmonicities. The pocket nature of the $T_{1u}$ gap and isotope modes is reflected in the fact that their amplitude patterns are strongly peaked at the defect's fourth neighbors—thus, for these modes, the amplitudes on the (200) sites are a factor of $\sim 5$ larger than the next

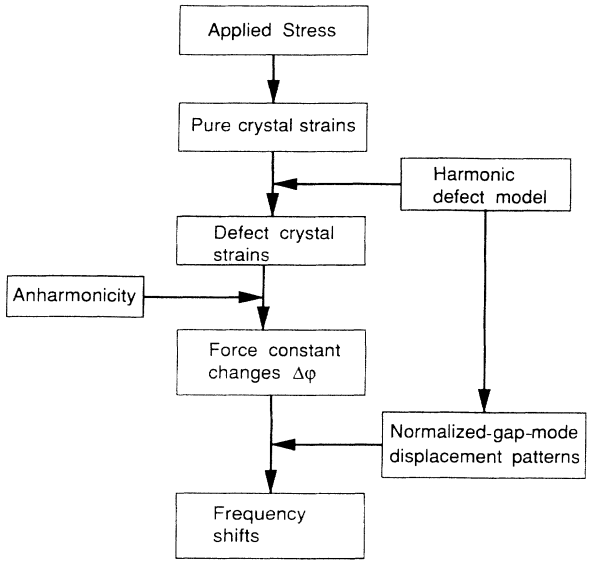


FIG. 9. Schematic diagram illustrating the procedure for calculating the stress coupling coefficients of the KI:$Ag^+$ ir-active pocket gap modes. Note that the defect-crystal strains and gap-mode displacements are both determined from the perturbed harmonic theory. The anharmonicity is only needed to determine the force-constant changes produced by the harmonic-defect-crystal local strains.

TABLE V. Theoretical and experimental resonant- and gap-mode frequencies for KI:$Ag^+$, together with $^{39}K^+ \rightarrow {}^{41}K^+$ (200) pocket-gap-mode isotope shifts, for the force-constant changes ($\delta$,$\delta'$) discussed in the text, compared with experiment. The model predicts the relative intensity for the $T_{1u}$ resonant and gap modes to be $S(86.2)/S(17.3)=1.4$ (the experimental value is 3) and the relative intensity for the $^{41}K/^{39}K$ (200) pocket gap modes to be $S(84.5)/S(86.2)=0.07$ (the experimental value is 0.04). The force-constant changes are given as fractions of the KI nearest-neighbor longitudinal overlap (shell-shell) force constant, $k=18.84$ N/m, of the breathing-shell model (Ref. 11). All frequencies are given in $cm^{-1}$.

| $\delta/k$ | $\delta'/k$ | $T_{1u}$ resonant | $T_{1u}$ gap | $E_g$ resonant | Isotope shift |
|---|---|---|---|---|---|
| $-0.563$[a] | $-0.528$[a] | 17.3 | 86.2 | 20.5 | $-1.5$ |
| Experiment[a] | | 17.3 | 86.2 | 16.1 | $-1.7$ |

[a]From Ref. 13. The value of $\delta/k$ differs slightly from the value ($-0.564$) given in Ref. 11 because the $T_{1u}$ gap-mode frequency has been found to be 86.2 $cm^{-1}$ in higher-resolution measurements (compared to the value of 86.3 $cm^{-1}$ given in Ref. 11).

largest amplitudes, which occur at the (300) sites [see Fig. 1(c)]. Even though these modes are strongly peaked on the (200) sites, we find it necessary to include displacements from several other sites, such as the (300), (400), and "pocket second-neighbor" sites (101) and (301), in our stress calculations. We have included a total of 72 sites in our calculations for the $T_{1u}$ 86.2-$cm^{-1}$ pocket gap mode and a total of 34 sites in our calculations for the (200) pocket isotope mode. Estimates using pure-crystal strains and calculated displacements show that our resulting values of the anharmonic parameters obtained by fitting the experimental stress data would change by less than 7% if we included displacements at additional sites. Considering that the defect- and pure-crystal strains are found to differ by less than 2% a few sites away from the defect, these error estimates should be accurate.

The (200) pocket isotope mode's largest displacements are confined to the pocket in the (100) direction. In contrast, the $\hat{x}$-polarized $T_{1u}$ pocket gap mode has large displacements in the pockets in both the (100) and (−100) directions. This difference accounts for some of the extra sites included in our stress calculations for the $T_{1u}$ pocket mode, but which are not needed in our stress calculations for the pocket isotope mode. Beyond this, the $T_{1u}$ pocket-gap-mode stress calculations require the inclusion of *additional* sites, such as (020) and (030), in non-(100) directions, in order to determine the $T_{2g}$ strain-induced coupling between the degenerate unperturbed $T_{1u}$ pocket modes. In our perturbation approach, such coupling does not occur for the isotope modes; hence, the inclusion of these additional sites is not needed for the isotope-mode stress calculations.

Since we assume central potentials, the defect's crystal symmetry reduces to 9 the number of independent cubic anharmonic coefficients needed to determine the force-constant changes between the (200) site and its nearest neighbors. Only six of the nine coefficients are needed to calculate the stress-induced frequency shifts:

$$A_1 \equiv \Phi_{xxx}(100,100,200), \quad A_2 \equiv \Phi_{xxx}(200,200,300) ,$$

$$B_1 \equiv \Phi_{yxy}(100,100,200), \quad B_2 \equiv \Phi_{xxz}(200,200,201) ,$$

$$B_3 \equiv \Phi_{yxy}(200,200,300), \quad C_2 = \Phi_{xxx}(200,200,201) .$$

These coefficients are appropriate to the unstressed defect-crystal equilibrium configuration.

In our perturbed-phonon model, only the (000)-(100) and (100)-(200) longitudinal force constants are perturbed; thus, we will treat $A_2$, $B_2$, $B_3$, and $C_2$ as for the pure crystal. In the pure crystal, point symmetry and the central potential assumption lead to $C_2 \equiv 0$ and $B_3 \equiv B_2$. Moreover, $B_2$ involves just $V'(r)$ and $V''(r)$, both of which may be obtained from the known nearest-neighbor overlap (shell-shell) force constants of the BSM,[12] together with the Coulomb interaction. This gives $B_2 = 2.02 \times 10^{11}$ dyn/$cm^2$. Knowing $B_2$, we then have three unknown independent anharmonic parameters, namely, $A_1$, $A_2$, and $B_1$.

### B. Anharmonic fit to the stress data

Our three independent anharmonic parameters can be fit to the measured stress coefficients $A$, $B$, and $C$. The first row of Table VI gives the results of fitting these anharmonic parameters to the stress coefficients for the 86.2-$cm^{-1}$ gap mode.[30] If we then use these values of $A_1$, $A_2$, and $B_1$, obtained by fitting the 86.2-$cm^{-1}$ $T_{1u}$ pocket-gap-mode stress data, to compute $A$, $B$, and $C$ for the $^{41}K^+$ (200) isotope mode, we obtain $A = 186$ $cm^{-1}$ and $B = 7$ $cm^{-1}$, in good agreement with the experimental results of Table IV. Given the pocket nature of the $T_{1u}$ gap and isotope modes, it is not surprising that they have such similar $A$ and $B$ stress coefficients. The stress coefficient $C$ describes the coupling between degenerate $T_{1u}$ modes produced by $T_{2g}$ strains; however, as pointed out in the description of our stress model, there is no such coupling for the isotope mode. Hence, in our model, $C$ should be identically zero for this mode, also in agreement with the experimental results.

### C. Comparison between the fit and simple potential models

At this stage, our anharmonic model amounts to a parametrization of the data; an assessment is needed as to the reasonableness of our fit values for $A_1$, $A_2$, and $B_1$. Given the many simplifying assumptions of the model (e.g., the neglect of the effects of defect-induced static distortions beyond the defect's fourth neighbors), we will compare with values obtained using a simple Born-Mayer[31] plus Coulomb nearest-neighbor potential

$$V(r) = \lambda e^{-r/\rho} - \frac{(0.9e)^2}{r} , \tag{2}$$

where $0.9e$ is the BSM value of the ionic charge and, for consistency, the KI Born-Mayer parameters are computed from the KI BSM shell-shell force constants ($\rho = 0.260$ Å, $\lambda = 8.47 \times 10^{-8}$ erg). To determine $A_1$ and $B_1$, we first combine this potential with our perturbed harmonic force-constant change $\delta'$ between the (100) and (200) ions, to compute the relaxed equilibrium separation between these ions, and then evaluate the first, second, and third derivatives of $V(r)$ at this separation. Since relaxation beyond the (200) ions is neglected in our model, the remaining anharmonic coefficients follow directly from potential derivatives evaluated at the host-crystal equilibrium separation. Our resulting values for $A_1$, $A_2$, and $B_1$ are given in the second row of Table VI, and they are seen to disagree with the fit values. The replacement of the Born-Mayer potential by a power-law potential for the overlap interaction yields no improvement.

TABLE VI. Anharmonic parameters $A_1$, $A_2$, and $B_1$ determined from the experimental 86.2-$cm^{-1}$ gap-mode stress coefficients $A$, $B$, and $C$, and from the Coulomb plus Born-Mayer (BM) potential fit to the harmonic-defect model. The units are $10^{12}$ dyn/$cm^2$.

| | $A_1$ | $A_2$ | $B_1$ |
|---|---|---|---|
| Fit to experiment | 6±1 | −17±3 | 3±4 |
| BM | −2.24 | −6.48 | −0.0812 |

TABLE VII. Stress coupling coefficients $A$, $B$, and $C$ for the 86.2-cm$^{-1}$ gap mode, as determined from the Coulomb plus Born-Mayer (BM) potential fit to our harmonic-defect model, compared with the experimental results of Table IV. The units of $A$, $B$, and $C$ are cm$^{-1}$/unit strain.

| | $A$ | $B$ | $C$ | $B/A$ |
|---|---|---|---|---|
| BM | 216 | 92 | −1.8 | 0.43 |
| Experiment | 186±21 | 9±6 | −7±6 | 0.05±0.03 |

In addition to comparing our Born-Mayer values of $A_1$, $A_2$, and $B_1$ with the fit values, it is instructive to use the Born-Mayer values to predict the stress coupling coefficients $A$, $B$, and $C$. These results are given in Table VII. The very unusual measured stress dependence for the KI:Ag$^+$ pocket gap and isotope modes seen in the experiments is reflected in the small measured value, $\sim 0.05$, of the ratio $B/A$. In contrast, the $B/A$ ratio of 0.43 predicted by the Born-Mayer anharmonicities is typical of that seen for standard impurity systems (e.g., Cl$^-$, Rb$^+$, and Cs$^+$ in KI; see Table IV).

The most striking difference between our fit values for $A_1$ and $A_2$ and their Born-Mayer counterparts is that the values for $A_1$ have opposite signs (see Table VI). The fit value for $A_1$ implies that the (100)-(200) longitudinal force constant *weakens* when the (100)-(200) distance decreases under stress. By contrast, the Born-Mayer value predicts that this force constant should strengthen when the distance decreases. If the (100)-(200) interaction is correctly described by *any* rapidly varying, strong repulsive potential plus a weaker attractive Coulomb potential, the force constant should strengthen when the (100)-(200) separation decreases. Thus our positive fit value of $A_1$ might be thought to imply that the attractive Coulomb term dominates the potential. However, even if we neglect the repulsive term altogether, the defect-induced relaxation would need to decrease the (100)-(200) separation by $\sim 40\%$ of the pure-crystal separation to reproduce our fit $A_1$ value. Clearly, this is an unreasonably large relaxation. In contrast, the Born-Mayer potential combined with $\delta'$ predicts a more reasonable 7.2% defect-induced decrease in the (100)-(200) separation. Hence an anomalously weak repulsive interaction is not a likely cause of the unusual experimental stress results.

## V. DISCUSSION

The results in Table IV show that the most striking difference between the stress coefficients of the KI:Ag$^+$ pocket gap modes and those of gap modes of standard defect systems is the very small measured value of $B$ for the former. In our model it is the weakening of the (100)-(200) force constant under $E_g$ stress which results in the small values of $B$ for the pocket modes. As shown in Table VIII, under an $E_g$ stress, the (100)-(200) distance decreases. With $A_1 > 0$, this decrease produces a weakened (100)-(200) force constant. This weakening of the (100)-(200) force constant partially cancels the stress-induced stiffening of the other force constants which determine the $T_{1u}$ pocket-gap-mode frequency, leading to a small frequency shift for these modes under $E_g$ stress. The differences between the $A_{1g}$ and $E_g$ strain patterns suggest a mechanism for weakening the (200)-(300) force constant that can also partially cancel the stiffening of the other force constants, but does not require the presence of the anomalous $A_1 > 0$ anharmonicity. Because of the substantial force-constant weakening between the (000)-(100) and (100)-(200) sites in our model, an $E_g$ stress applied to KI:Ag$^+$ produces a *smaller* decrease in the (200)-(300) separation than that observed in the pure crystal, as shown in Table VIII. A similar but smaller effect occurs under an applied $A_{1g}$ stress. When we further weaken the force constant $\delta'$ between the (100) and (200) sites beyond our ir fit point, the separation between the (200) and (300) ions eventually *increases* when subjected to an $E_g$ stress. When coupled with "normal," i.e., repulsive-dominated, anharmonicity, this leads to a stress-induced anharmonic weakening of the (200)-(300) force constant, which partially compensates for the stress-induced stiffening of the other force constants and produces the small frequency shift observed for $E_g$ stress.

However, changing the $\delta'$ force constant changes the defect-model fit to the low-temperature ir and Raman spectra. We have found that we cannot obtain a reasonable fit to the ir and Raman spectra with a weak enough force constant $\delta'$ to produce the above strain effect. If the strain effect is, in fact, the correct explanation, this suggests that we need to include additional force-constant changes in our harmonic model in order to accurately describe the low-temperature spectra and simultaneously produce the unusual $E_g$ strain pattern.

TABLE VIII. Calculated $E_g(1)$ stress-induced relative displacements $\Delta r(l,m)$ per unit stress along (100) between the $l$th and $m$th sites for the pure crystal and for our defect model, in units of $10^{-19}$ cm$^3$/dyn. Note that the (300)-(200) separation changes less in the defect crystal than in the pure crystal.

| | $\Delta r$(200,100) | $\Delta r$(300,200) | $\Delta r$(400,300) |
|---|---|---|---|
| Pure crystal | −0.55 | −0.55 | −0.55 |
| KI:Ag$^+$ (harmonic-defect model) | −1.0 | −0.27 | −0.43 |

## VI. CONCLUSIONS

The unusual nature of the stress dependence measured for the KI:Ag$^+$ pocket gap modes is demonstrated in Table IV: Whereas standard gap modes (e.g., KI:Cl$^-$, KI:$F$ center, KI:Cs$^+$, and KI:Rb$^+$) are coupled strongly to both fully symmetric and tetragonal strains, as reflected by the comparable values of the $A$ and $B$ coupling coefficients, the KI:Ag$^+$ pocket gap and isotope modes, as well as the 55.8-cm$^{-1}$ band mode, have similar $A$'s, but nearly vanishing $B$'s; thus, these three modes couple almost exclusively to fully symmetric strains. The ratio of the coupling coefficients $B/A$ (see the last column in Table IV) of the previously measured KI:Ag$^+$ low-frequency resonant mode is more similar to the $B/A$ values of the standard gap modes than to those of the KI:Ag$^+$ pocket gap and isotope modes, and of the 55.8-cm$^{-1}$ mode. This suggests that a small $B/A$ ratio may

be a stress-behavior signature of the pocket nature of a mode.

An interesting question raised by these results concerns the lattice-dynamical origin of the 55.8-$cm^{-1}$ KI:$Ag^+$ mode. This anomalously sharp but weak mode inside the high-density-of-states acoustic-phonon region is found to share the unique uniaxial-stress behavior of the pocket modes, suggesting that it in turn may also have a pocket-type displacement pattern. However, there is no evidence of any such mode in the defect-induced $T_{1u}$ spectrum calculated from the harmonic shell model, which successfully predicted the pocket gap mode and its isotope effect. Thus the origin of the 55.8-$cm^{-1}$ KI:$Ag^+$ line remains an open question.

In trying to explain the unique pocket-mode stress behavior, we have consistently extended our harmonic model for the low-temperature dynamics of KI:$Ag^+$ to describe the ir-active gap-mode frequency shifts under uniaxial stress. We were able to fit the cubic anharmonic terms between the (200) site and its nearest neighbors to the experimental stress data. However, our fit anharmonicity $A_1$ between the (100) and (200) sites is anomalous if the interaction between these ions is described by the usual strong rapidly varying repulsive potential with a weaker Coulomb potential.

The computed stress-induced displacement patterns point toward another possible explanation of the unusual stress coefficients observed for the $T_{1u}$ pocket gap modes, without requiring anomalous anharmonicity. If the (100)-(200) longitudinal force constant in our defect model for the low-temperature dynamics were weakened beyond the value we obtained by fitting the $T_{1u}$ gap and resonant modes, the (200)-(300) separation would actually increase under an $E_g$ stress, in contrast to the decrease which occurs in the pure crystal. If the (200)-(300) potential were dominated by a standard strong repulsive term, this increase in the separation would weaken the (200)-(300) longidinal force constant under stress, thus partially compensating for the stress-induced stiffening of other force constants. This could produce a small $B$ value, such as that observed experimentally. However, changing the defect-model force constant would change the predicted far-ir and Raman spectra. Varying just the two force constants we have used to fit the far-ir data, we were not able to maintain a reasonable fit to the low-temperature far-ir and Raman spectra with weak enough force constants to produce this strain effect. This suggests that we need to include additional force-constant changes in our model in order to describe the far-ir and Raman spectra *and* to produce the unusual $E_g$ strain pattern suggested by the measured stress coefficients.

We have seen that the fit values for the anharmonic coefficients are anomalous when compared with coefficients obtained within our model using simple potentials. Given the uncertainties in the validity of simple phenomenological potentials over a wide range of defect-induced static displacements, it would be desirable to have a test for our fit anharmonic coefficients which avoids any use of potentials. A theory analogous to that used here for the stress-induced shifts can be developed to relate the anharmonicity to the frequency shifts and mixing of the pocket gap modes produced by an applied static *electric* field. Since the "strains" produced by such a field should be markedly different from the stress-induced strains, the stress and electric-field experiments together can provide a direct test of the model, with no use of potentials whatsoever.

## ACKNOWLEDGMENTS

C. E. Mungan would like to thank G. Schmidt for instruction in the growth of doped alkali halide crystals. We thank Dr. K. Muro for the design of the stress apparatus. Work by A.R., C.E.M., and A.J.S. is supported by Grants Nos. NSF-DMR-89-18894 and ARO-DAAL03-90-G-0040. We also acknowledge the crystal growing facility support through the Cornell Materials Science Center under Grant No. NSF-DMR-88-18558-A02. Work by K.W.S. and J.B.P. is supported by Grants Nos. NSF-DMR-90-12143 and NSF-DMR-90-14729. J.B.P. gratefully acknowledges the support of the Alexander von Humboldt Foundation and the Institute for Theoretical Physics, University of Regensburg, Germany, during a portion of this work.

## APPENDIX: STRESS-SHIFT THEORY

In the main text, we gave a qualitative outline of how we extended our harmonic model to describe the pocket-gap-mode stress-induced shifts. Here we present a more detailed discussion of how this was done.

In the presence of external forces, the equations of motion for $N$ ions interacting via harmonic forces is

$$\underline{M}\ddot{\mathbf{u}}=\underline{\Phi}\mathbf{u}+\mathbf{F}_{\text{ext}} , \tag{A1}$$

where $\mathbf{u}=\{u_\alpha(l)\}$ is the $3N$-dimensional vector containing the ion displacements from their equilibrium positions, $\underline{\Phi}=\{\Phi_{\alpha\beta}(l,m)\}$ is the harmonic force-constant matrix, $\underline{M}=\{M_l\delta_{lm}\delta_{\alpha\beta}\}$ is the diagonal mass matrix, and $\mathbf{F}_{\text{ext}}=\{F_\alpha(l)\}$ contains the external forces acting on each of the ions. Here, $l,m=1,\ldots,N$ label the ion sites, while $\alpha,\beta=x,y,z$ denote Cartesian components.

When identical stresses are applied to the defect and pure crystals, the stress-induced static displacement $\xi$ for the defect crystal can be related to the pure-crystal stress-induced displacements $\xi_0$ by solving Eq. (A1) for the external forces and equating the resulting pure- and defect-crystal expressions to yield[29]

$$\xi=[\underline{I}+\underline{G}_0(0)\underline{C}]^{-1}\xi_0 . \tag{A2}$$

This matrix equation can be partitioned into two equations: one involving displacements and matrix elements inside the defect space determined by the harmonic-defect model's perturbed mass and force-constant changes, and a second which determines the displacements outside the defect space. These equations are

$$\xi_I=(\underline{I}_{II}+\underline{G}_{0II}\underline{C}_{II})^{-1}\xi_{0I} \tag{A3}$$

and

$$\xi_R=-\underline{G}_{0RI}\underline{C}_{II}\xi_I+\xi_{0R} , \tag{A4}$$

where $\underline{G}_0(\omega^2)=(\underline{\Phi}_0-\omega^2\underline{M}_0)^{-1}$ is the harmonic Green's function for the pure crystal and $\underline{C}=\Delta\underline{\Phi}-\omega^2\Delta\underline{M}$ contains the defect-induced mass change and force-constant

changes $\Delta\underline{M}$ and $\Delta\underline{\Phi}$, respectively. The $I$ and $R$ subscripts refer to components inside and outside the defect space, respectively. If the defect space is small, which is expected to be the case for isoelectronic point defects, one can readily solve Eq. (A3) to determine the defect-space ion displacements from the pure-crystal stress-induced displacements and the defect-space Green's function elements. Equation (A4) then determines the defect-crystal stress-induced displacements outside the defect space. Because of the localized nature of the gap modes, we only need a limited number of stress-induced displacements outside the defect space to determine the stress-induced frequency shifts.

In order to determine the Green's-function elements needed for Eqs. (A3) and (A4), the static Green's function can be rewritten as $\underline{G}_0(0)=\sum_f \chi(f)\tilde{\chi}(f)/\omega_f^2$, where $\chi(f)$ is the $3N$-dimensional normal-mode displacement pattern for mode $f$ ($f=1,\ldots,3N$) with frequency $\omega_f$, normalized according to $\tilde{\chi}(f)\underline{M}_0\chi(f)=1$. For the pure crystal, the normal modes are plane waves and the $\chi$'s are complex: $\chi_\alpha(Lb|\mathbf{k}j)\propto e_\alpha(b|\mathbf{k}j)\exp[-i\mathbf{k}\cdot\mathbf{R}(Lb)]$, where the $\{e_\alpha(b|\mathbf{k}j)\}$ are components of the polarization vector, $\mathbf{k}$ is the wave vector, $j$ labels the branch, and $\mathbf{R}(Lb)$ is the equilibrium position for the $(Lb)$ ion, with $b$ specifying a particular atom in unit cell $L$. A given Green's-function element $G_{0\alpha\beta}(l,m)$ can be calculated by directly summing over the pure-crystal normal modes determined by the breathing-shell model.

The pure-crystal stress-induced displacements can be obtained directly from elasticity theory as

$$\xi_{0\alpha}(l)=\tfrac{1}{2}\sum_{\beta\neq\alpha} R_\alpha(l)\varepsilon_{\alpha\beta}+R_\alpha(l)\varepsilon_{\alpha\alpha} . \tag{A5}$$

Here $\varepsilon_{\alpha\beta}$ are the pure-crystal elastic strains and $\mathbf{R}(l)$ is the equilibrium position for the $l$th ion measured relative to the ion at the origin, which does not move under stress. The sum in Eq. (A5) is extended beyond the six independent elastic strains by using the identity $\varepsilon_{\alpha\beta}=\varepsilon_{\beta\alpha}$. The six independent elastic strains $(\varepsilon_{xx},\varepsilon_{yy},\varepsilon_{zz},\varepsilon_{xy},\varepsilon_{xz},\varepsilon_{yz})$ are related to the crystal stresses $\underline{\sigma}$ by

$$\varepsilon_{\alpha\beta}=\sum_{\gamma\delta} S_{\alpha\beta,\gamma\delta}\sigma_{\gamma\delta} , \tag{A6}$$

where $\underline{S}$ is a fourth-rank tensor of crystal compliances and $\alpha,\beta,\gamma,\delta$ are Cartesian indices.

Under an applied stress, the ions' equilibrium positions shift in the manner described above. In a purely harmonic crystal, these displacements would not change the force constants. However, in the presence of anharmonicity, we need to expand the potential energy about the new equilibrium positions to determine the new force constants. To lowest order in the stress-induced displacements, the corrections to the unperturbed defect-crystal force constants are

$$\delta\Phi_{\alpha\beta}(l,m)=\sum_{n\gamma}\Phi_{\alpha\beta\gamma}(l,m,n)\xi_\gamma(n) , \tag{A7}$$

where the $\Phi_{\alpha\beta\gamma}(l,m,n)$ are the cubic anharmonic coefficients.

The frequencies and displacement patterns for the normal modes of a harmonic crystal are determined by the matrix equation

$$(\underline{\Phi}-\omega_f^2\underline{M})\chi(f)=\mathbf{0} . \tag{A8}$$

To determine the frequency shifts produced by the stress-induced force-constant changes, we treat the force-constant changes as small and do a perturbation expansion of the mode-displacement patterns and frequencies. Substituting these expansions into Eq. (A8), we obtain the lowest-order squared frequency shift for a nondegenerate mode as

$$\Delta\omega_f^2=\tilde{\chi}(f)\delta\underline{\Phi}\chi(f) . \tag{A9}$$

In the present study, the isotope gap mode is separated by $\sim 1.5$ cm$^{-1}$ from the other gap modes; this is a large separation compared to the stress-induced frequency shifts. Thus nondegenerate perturbation should apply to this mode. By contrast, the $T_{1u}$ ir-active pocket gap mode is threefold degenerate, and so we need to use degenerate perturbation theory to calculate the stress-induced frequency shifts for these modes. This yields

$$(\underline{A}-\Delta\omega^2\underline{I})\mathbf{a}=\mathbf{0} , \tag{A10}$$

where $A_{ff'}=\tilde{\chi}(f)\delta\underline{\Phi}\chi(f')$ are the components of the $3\times3$ matrix $\underline{A}$ coupling the degenerate $T_{1u}$ modes, and the components of the eigenvector $\mathbf{a}$ determine the zeroth-order displacement patterns $\psi$ as linear combinations of the three $T_{1u}$ gap modes; $\psi=\sum_f a_f\chi(f)$, where the sum only runs over the three $T_{1u}$ modes. We will take $x,y,z$-polarized $T_{1u}$ gap modes as the basis for the degenerate perturbation calculation. Even though the $E_g$ and $A_{1g}$ pocket gap modes are nearly degenerate with the $T_{1u}$ gap modes, they are not involved in this calculation because the stress-induced strains do not couple odd- and even-parity modes.

Using symmetry arguments similar to those used by Gebhardt and Maier,[25] we can rewrite the matrix $\underline{A}$ coupling the $T_{1u}$ modes as

$$\underline{A}=2\omega_{T1u}P\begin{vmatrix} A(S_{11}+2S_{12}) & & \\ +2B(S_{11}-S_{12})(2\alpha^2-\beta^2-\gamma^2) & CS_{44}\alpha\beta & CS_{44}\alpha\gamma \\ & A(S_{11}+2S_{12}) & \\ CS_{44}\alpha\beta & +2B(S_{11}-S_{12})(2\beta^2-\alpha^2-\gamma^2) & CS_{44}\beta\gamma \\ & & A(S_{11}+2S_{12}) \\ CS_{44}\alpha\gamma & CS_{44}\beta\gamma & +2B(S_{11}-S_{12})(2\gamma^2-\alpha^2-\beta^2) \end{vmatrix} , \tag{A11}$$

where $\alpha$, $\beta$, and $\gamma$ are the $x$-, $y$-, and $z$-direction cosines, respectively, of the applied uniaxial stress of magnitude $P$ and $\omega_{T1u}$ is the unperturbed $T_{1u}$ gap-mode frequency. The stress coefficients $A$, $B$, and $C$ couple the $T_{1u}$ modes to $A_{1g}$, $E_g$, and $T_{2g}$ stresses, respectively. These coefficients can be determined easily by calculating the matrix elements of $\underline{A}$ for various directions of the applied stress (see Table III).

The stress coefficients $A$ and $B$ coupling the *isotope* pocket gap mode to $A_{1g}$ and $E_g$ stresses can also be determined. For a (200) $^{41}K^+$ isotope mode, we obtain

$$\Delta\omega_f^2=\tilde{\chi}(f)\delta\underline{\Phi}\chi(f)$$
$$=2\omega_{T1u}P[\,A(S_{11}+2S_{12})$$
$$+2B(S_{11}-S_{12})(2\alpha^2-\beta^2-\gamma^2)]\,. \quad \text{(A12)}$$

Here $\chi(f)$ is the normalized *isotope*-mode-displacement pattern. The stress-induced (200) isotope-mode splitting has the same form as the splitting predicted for the $\hat{x}$-polarized $T_{1u}$ pocket gap mode, except that $C=0$.


[1]A. S. Barker and A. J. Sievers, Rev. Mod. Phys. **47**, Suppl. 2, S1 (1975).

[2]R. D. Kirby, A. E. Hughes, and A. J. Sievers, Phys. Rev. B **2**, 481 (1970).

[3]S. Kapphan and F. Lüty, Phys. Rev. B **6**, 1537 (1972).

[4]F. Bridges, Phys. Rev. B **5**, 3321 (1972).

[5]F. Bridges, CRC Crit. Rev. Solid State Sci. **5**, 1 (1975).

[6]U. Holland and F. Lüty, Phys. Rev. B **19**, 4298 (1979).

[7]F. Bridges and D. Chow, Phys. Rev. Lett. **54**, 1532 (1985).

[8]F. Bridges and M. Jost, Phys. Rev. B **38**, 12 105 (1988).

[9]A. J. Sievers and L. H. Greene, Phys. Rev. Lett. **52**, 1234 (1984).

[10]S. B. Hearon and A. J. Sievers, Phys. Rev. B **30**, 4853 (1984).

[11]J. B. Page, J. T. McWhirter, A. J. Sievers, H. Fleurent, A. Bouwen, and D. Schoemaker, Phys. Rev. Lett. **63**, 1837 (1989).

[12]U. Schröder, Solid State Commun. **4**, 347 (1966).

[13]K. W. Sandusky, J. B. Page, A. Rosenberg, C. E. Mungan, and A. J. Sievers, Phys. Rev. Lett. **67**, 871 (1991).

[14]I. G. Nolt and A. J. Sievers, Phys. Rev. **174**, 1004 (1968).

[15]We used Johnson Matthey Puratronic KI, the highest-purity grade available from this manufacturer. This material has some $Cl^-$ and $Cs^+$, but no measurable $Rb^+$, as naturally occurring impurities. We have found that less-pure types of KI from Aesar, Alpha and Johnson Matthey contain naturally occurring $Rb^+$, whose gap modes interfere with the KI:$Ag^+$ gap modes.

[16]The linewidths ($\Gamma$) reported in this paper are given by $\Gamma=(\Gamma_m^2-\Gamma_i^2)^{1/2}$, where $\Gamma_m$ is the measured FWHM of the line and $\Gamma_i$ is the instrumental resolution.

[17]F. Agullo-Lopez, C. R. A. Catlow, and P. D. Townsend, *Point Defects in Materials* (Academic, New York, 1988), Chap. 4.

[18]D. Labrie, I. J. Booth, M. L. W. Thewalt, and B. P. Clayman, Appl. Opt. **25**, 171 (1986).

[19]W. P. Ambrose, Ph.D. thesis, Cornell University, 1989.

[20]We used UHU Plus Endfest 300 epoxy and Cerrolow-117 solder (with a melting point of 47 °C) obtained from the Cerro Metal Products Co. The polypropylene film was obtained from Hercules Inc.

[21]R. D. Kirby, Phys. Rev. B **4**, 3557 (1971).

[22]H. Bilz and W. Kress, *Phonon Dispersion Relations in Insulators* (Springer-Verlag, Berlin, 1979), p. 43.

[23]S. P. Love, W. P. Ambrose, and A. J. Sievers, Phys. Rev. B **39**, 10 352 (1989).

[24]C. E. Mungan, R. C. Spitzer, J. P. Sethna, and A. J. Sievers, Phys. Rev. B **43**, 43 (1991).

[25]W. Gebhardt and K. Maier, Phys. Status Solidi **8**, 303 (1965).

[26]M. H. Norwood and C. V. Briscoe, Phys. Rev. **112**, 45 (1958).

[27]A. M. Kahan, M. Patterson, and A. J. Sievers, Phys. Rev. B **14**, 5422 (1976).

[28]D. Bäuerle and R. Hübner, Phys. Rev. B **2**, 4252 (1970).

[29]R. J. Elliot, J. A. Krumhansl, and T. H. Merrett, in *Localized Excitations in Solids*, edited by R. F. Wallis (Plenum, New York, 1968), p. 709.

[30]In our model we have treated $A_2$ as a pure-crystal anharmonic parameter. The fit to the pocket-gap-mode stress data produces $A_2=(-1.7\pm0.3)\times10^{13}$ dyn/cm$^2$. This coefficient differs by a factor of $\sim4$ from the value determined from a quasiharmonic model fit to pure KI thermal expansion [M. S. Haque, Phys. Rev. B **12**, 1501 (1975)]. In our harmonic model, we have included a large (100)-(200) longitudinal force-constant change ($\delta'$), which we assume to be produced by defect-induced inward relaxation of the (100) ion. If the (100) ion moves inward, it is reasonable to suppose that the (200) ion also relaxes. In this case the (200)-(300) separation changes and $A_2$ would no longer correspond to a pure-crystal quantity. If we modify our model and use the pure-crystal anharmonic parameter determined by fitting the thermal-expansion data everywhere in our calculation that the pure crystal $A_2$ coefficient occurs, except between the (200) and (300) sites, our fit values for $A_1$ and $A_2$ increase by roughly a factor of 3, but keep the same sign. As is argued in Sec. IV C, $A_1\geq0$ is anomalous. The factor of 3 increase in these modified fit values of $A_1$ and $A_2$ does not remove the anomaly.

[31]M. Born and K. Huang, *Dynamical Theory of Crystal Lattices* (Oxford University Press, London, 1956).

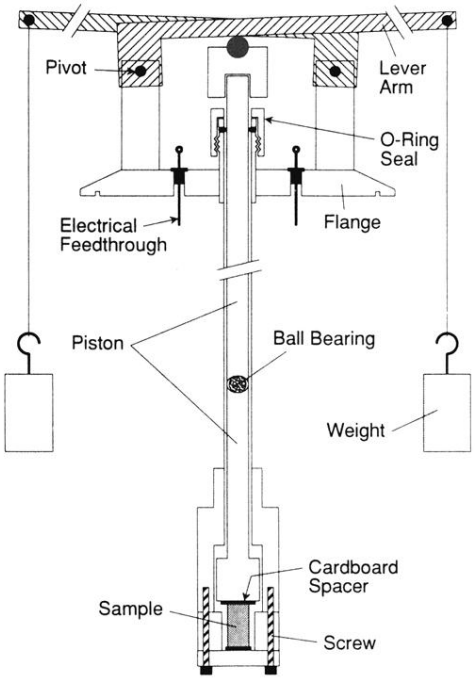


FIG. 3. Schematic view of the uniaxial-stress cryostat insert. The weights hang on lever arms external to the cryostat. The flange seals the top of the cryostat sample chamber. The force is transmitted to the sample by a piston which enters the cryostat through an o-ring seal. Cardboard spacers are used on the top and bottom of the sample to distribute the pressure uniformly. An electrical feedthrough allows temperature measurements by connecting to a calibrated carbon resistor near the sample. The total length of the insert is $\sim 1$ m (not to scale).